HHS Public Access

Author manuscript

Adv Funct Mater. Author manuscript; available in PMC 2025 April 30.

Published in final edited form as:

Adv Funct Mater. 2024 October 08; 34(41): . doi:10.1002/adfm.202400842.

Modular Anti-Counterfeit Tags Formed by Template-Assisted Self-Assembly of Plasmonic Nanocrystals and Authenticated by Machine Learning

Maha Ibrar,
Department of Chemistry, Indiana University, Bloomington, IN 47405, USA

Sheng-Yuan Huang,
Department of Chemistry, Indiana University, Bloomington, IN 47405, USA

Zachery McCurtain,
Department of Computer Science, Indiana University, Bloomington, IN 47405, USA

Shujon Naha,
Department of Computer Science, Indiana University, Bloomington, IN 47405, USA

David J. Crandall,
Department of Computer Science, Indiana University, Bloomington, IN 47405, USA

Stephen C. Jacobson,
Department of Chemistry, Indiana University, Bloomington, IN 47405, USA

Sara E. Skrabalak
Department of Chemistry, Indiana University, Bloomington, IN 47405, USA

Abstract

Counterfeit goods are pervasive, being found in products as diverse as textiles and optical media to pharmaceuticals and sensitive electronics. Here, an anti-counterfeit platform is reported in which plasmonic nanoparticles (NPs) are used to create unique image tags that can be authenticated quickly and reliably. Specifically, plasmonic NPs are assembled into periodic arrays of NP clusters by template-assisted self-assembly (TASA), where the light scattering responses from the arrays are analyzed by dark-field optical microscopy. Tag design proved modular as plasmonic NPs with different optical responses can be selected and paired with Templates with different features

sskrabal@indiana.edu .

Author Contributions

M.I. and S.S. were responsible for the design of this project. M.I. was responsible for the synthesis and characterization of plasmonic NPs, creation of tags, and optical microscopy and data analyses. S.C.J. and S.-Y.H. developed and optimized the fabrication method for the Templates. S.-Y.H. fabricated and characterized the Templates and analyzed the data. Z.M. and S.N. designed and implemented image analysis algorithms and neural network training. D.C. supervised the design and implementation of all computer vision aspects of the project. All authors discussed the data and contributed to the writing of the manuscript.

Conflict of Interest

The authors declare no conflict of interest.

Supporting Information

Supporting Information is available from the Wiley Online Library or from the author.

(e.g., well size, well shape, and number and arrangement of wells in an array), giving access to a variety of color responses and unique images. These images can be differentiated from one another and authenticated by image analysis. Authentication methods based on shallow and deep neural networks are compared, where deep neural networks authenticated TASA tags with higher accuracy. Given the ease of tag fabrication and rapid image analysis, these platforms are ideal for on-the-fly tagging and supply-chain authentication of critical goods.

Keywords

artificial intelligence; gold nanocrystals; nanorods; plasmonics; template-assisted assembly

1. Introduction

Nanoscale materials offer unique and size-dependent properties for use in diverse applications.[1–6] A property of particular interest is the light scattering and absorption by metal nanoparticles (NPs). This optical response of metal NPs arises from their localized surface plasmon resonances (LSPRs) in which the electron clouds of metal NPs couple with incident light to create coherent, collective oscillations.[7,8] The energies of such resonances can be judiciously achieved by changing NP size, shape, composition, and their environment.[9–14] Here, the LSPRs of Au NPs are leveraged to create security tags when assembled into arrays.

Counterfeit items are infiltrating many industries and commercial goods, giving rise to economic losses, device reliability issues, and health and safety concerns.[15–17] The proliferation of non-genuine goods necessitates the development of anti-counterfeit platforms such as tags that provide quick, reliable, and cost-effective authentication, tracking and tracing of products, and detection of potential tamper activity.[18] Most tags rely on deterministic processes to create images or barcodes,[19–22] although our prior work produced physically unclonable functions from randomly deposited Au NPs that were covert to the unaided eye.[9,23] Physically unclonable functions can be achieved from a variety of plasmonic and fluorescent nanostructures, including hierarchical and dendritic structures, multilayered structures, and NPs in polymers, leading to large encoding capacities.[24–29] Regardless of the tag type, they must have fast and convenient readout while dissuading a counterfeiter who has figured out the tag design, so that radical changes to the tag design and fabrication process are not necessary.

Thus, impetus has been placed on fabrication of modular tags for quick tagging and screening of goods that are robust against reverse engineering attacks. We show herein that template-assisted self-assembly (TASA) with Au NP Inks addresses this need by creating unique images as tags for coarse-grained and quick analysis of goods. TASA controls the dispersion of NPs with a polymeric Template array that confines NPs to specified, well-defined regions of a substrate. The optical images created by TASA of NPs are defined by the dimensions of the array, the size and shape of the Template features (i.e., wells for NPs), and the size and shape of the NPs themselves. This tag design is robust against back-engineering from visual inspection of the tags. NP morphology as well as Template

dimensions can only be determined by electron microcopy of the tags, with well-depth not inferable from the tag itself. NP composition would require integration of spectroscopy with microscopic analysis. Additionally, the Ink formulation, which determines the quality of Template filling and, thus, tag, would only be known by the manufacturer. These features make tag replication practically impossible.

Arrays of metal NPs created by TASA have been studied for sensing, electrochemistry applications, and in structural color applications.[30–32] To the best of our knowledge, they have not been evaluated as security tags even though TASA-generated security tags from metal NPs could offer broad materials compatibility. That is, assemblies of NPs by TASA have been integrated into adhesive substrates (e.g., tapes or polydimethylsiloxane (PDMS) films) and non-adhesive substrates (e.g., glass slides, silicon wafers, and polyethylene terephthalate (PET) sheets), nanoporous semipermeable transparent membranes, and stretchable textiles.[33–36] This versatility means TASA could be optimized to create durable tags for a variety of critical goods, such as wearable devices, packaging and sealing materials, and sensitive microelectronics. As a first step toward validating TASA-generated NP arrays as security tags, we show that TASA of NP Inks is a modular approach to different optical security tags that can be readily classified and verified with image analysis and machine learning.

2. Results and Discussion

2.1. Tag Design and Preparation

The design and application of plasmonic security tags based on TASA of Au NPs consist of fabrication and authentication stages. Figure 1 shows that the fabrication of tags involves 1) the formulation of an NP Ink in parallel with the design and fabrication of Templates for TASA, followed by 2) creation of arrayed assemblies of NPs by TASA, and 3) their transfer to a surface (e.g., of a critical good) by lift-off from the Templates. 4) Finally, an image is collected of the scattering response from the NP array observed by dark-field optical microscopy with an interfaced colored CCD camera; the camera captures the color and position of scattering from each cluster of NPs. This image serves as the optical security tag that can be analyzed by an algorithm for authentication.

For proof-of-concept and to demonstrate the modular nature of this security tag approach, three aqueous Au NP solutions, i.e., Inks, were selected for tag fabrication: Ink A of Au nanorods with average length 67.3 ± 7.7 nm and width 19.2 ± 2.3 nm (aspect ratio = 3.5), Ink B of Au nanorods with average length 91.2 nm ± 10.1 nm and width 38.2 ± 4.2 nm (aspect ratio = 2.4), and Ink C of Au NPs with a quasi-spherical shape and average diameter of 68.8 nm ± 7.1 nm. TEM images, UV–vis spectroscopy results, and a summary of NP features are provided in Figures 2a and S1 as well as Table S1 (Supporting Information). See Supporting Information (SI) and Table S2 (Supporting Information) for details of their preparation. These solutions were selected because of the chemical inertness of Au NPs. Also, Au NPs have strong LSPRs that can be tuned throughout the visible region, with nanorods displaying longitudinal ($LSPR_L$) and transverse ($LSPR_T$) resonances that depend on their aspect ratio while quasi-spherical Au NPs display a single dipolar LSPR due to their high symmetry.[7,37–39] The anisotropy of Au NPs introduces a dependence on light

polarization, which can be leveraged to increase the encoding capacity of a tag. The $LSPR_L$ of Ink A is located at 695 nm, and that of Ink B is located at 625 nm, with both their $LSPR_T$ slightly red-shifted from 500 nm. Ink C has only a single dipolar resonance at 525 nm.

Five topographically patterned Templates with different features (Table 1) were used for TASA. Templates were fabricated by a double replication method (see Figure S2, Supporting Information for details).[40] The master was milled with a focused ion beam (FIB) into a glass substrate, an intermediate mold of the master was formed in a UV-curable polymer, OrmoStamp, and a replica of the mold was cast from the mold into highly cross-linked poly(dimethylsiloxane) (x-PDMS) and supported with a second pliable PDMS layer. These x-PDMS/PDMS replicas were then used as the Templates. Atomic force microscope (AFM) images of the glass masters are shown in Figures S3–S7 (Supporting Information). Template I consisted of circular wells with a diameter of 240 nm and depth of 66 nm; they are arranged in a 25×25 array with a 500 nm spacing between wells. Template II had triangular wells, instead of circular wells, with a base of 250 nm, height of 180 nm, and depth of 50 nm. Template III had wells with a smaller diameter and shallower depth than Template I whereas Templates IV and V differed from Template I with a different array size and well spacing.

Like the Inks, Templates were selected to demonstrate the modular nature of this security tag approach, where the different well and array features will give rise to different near- and far-field coupling effects, diversifying the optical responses from various tags. Near-field coupling occurs when NPs are relatively densely packed (e.g., in clusters), leading to spectral shifts of the plasmonic resonances due to the hybridization of the plasmonic modes.[41] Far-field effects prevail further away from the metal surface. For example, for NPs arranged in a periodic array, where the array period is comparable to the wavelength of the incident light, scattered fields impinging on a NP correspond to the diffraction of the incident light in the array plane.[42] By judiciously selecting the right NP size and appropriate array period, light scattered by each plasmonic unit can be organized to be in phase with the LSPR of its neighboring unit.[43] When extended to an array of plasmonic units, diffractively coupled LSPRs or plasmon surface lattice resonances reduce plasmon damping of a single particle response and enhance NP scattering.[44] For these tags, 500 nm was chosen as the standard period to maximize the lattice plasmon coupling,[45–47] where the surface plasmon lattice resonances can be further tuned by the properties of the plasmonic repeating unit (NP shape, composition, and orientation with respect to incident wave).[48] Hence, the first level of modularity in optical responses of plasmonic arrays is investigated by using different NP Inks while the second level of modularity comes from the geometric parameters of the Template and include size/shape of the repeating unit, array size and shape, and periodicity.[43]

Figure S8 (Supporting Information) further illustrates the modularity of the tag design and combinational possibilities enabled by TASA. The total number of combinations can be calculated by Equation 1, where I_i represents the number of Inks and T_i represents the number of Templates.

$$C = I_i X T_j \quad (1)$$

Theoretically, an unlimited number of Inks with variable NP morphologies and compositions can be combined with a multitude of Templates. However, selection of Inks and Templates must be judicious to avoid spectral overlap so distinct color combinations can be accessed. Previously, Au nanorods with $LSPR_L$ difference of 7 nm displayed a completely unique RGB distribution.[9] Color change at such a small spectral difference makes such plasmonic Inks ideal for the development of a modular system.

With the NP Inks and Templates prepared, the process for TASA is summarized in Figure S9 (Supporting Information) where 1) a drop of NP Ink is placed on the Template, 2) a clean glass substrate is placed on the Template at an optimized time after drop-casting, and 3) the solvent is allowed to dry overnight. Finally, 4) the substrate is lifted off the Template, transferring the NP array set by the Template to the substrate. We note that the glass substrate serves as a model surface but could be replaced with the surface of a critical good. Moreover, to achieve high-quality NP arrays by TASA (i.e., those with uniform clusters and few NPs between clusters), optimization of solvent/Ink conditions, substrate pre-treatment, and drying times is essential; the optimized conditions are summarized in the Supporting Information.

Figure 3 shows dark-field optical microscopy images and scanning electron microscope (SEM) images from TASA of Inks A-C (from top to bottom) as a function of the five Templates, designated as columns I–V. Optical microscopy of the tag created from TASA of Ink A with Template I shows a largely monochromatic response, with green spots dominating the response of the array. SEM imaging shows that many rods come together in each cluster, with each cluster being largely isotropic. The largely monochromatic response can be attributed to the formation of isotropic clusters. The tags created from TASA of Ink A with Templates II or III – triangular wells and circular wells of smaller dimension compared to Template I – led to fewer rods per cluster compared to Template I. Fewer rods per cluster gives rise to cluster anisotropy and more varied colorimetric responses when comparing one cluster spot to another. Expanding the array from 25 × 25 circular cluster spots as in Template I to a 100 × 100 array as in Template IV leads to a purple-blue color response, rather than green, despite having similar nanorod packing arrangements in the clusters. This change in colorimetric response can be attributed to different lattice surface plasmon interactions mixing structural color with the hybridized LSPRs from the nanorod clusters. Finally, tags created from TASA of Ink A with Template V, where the array spacings were larger compared to Template I, were notably dimmer, although the response was still largely green. The brightness of the tags is important to demonstrate how inter-cluster distances influence far-field coupling effects and structural color. An average brightness value of 93.7 arbitrary units (au) was obtained from Template I with Ink A compared to 36.1 au from Template V with Ink A (see Supporting Information on how these values were obtained). Qualitatively, these comparisons show that features of the Template (well size and shape)

and array (spacing and overall dimensions) can be changed to achieve different optical tags while keeping the Ink features constant.

The results from Ink A highlight the promise of TASA in creating optical security tags as varied color responses were obtained from different Templates. The possibility of tag redesign was also evaluated by selecting different Inks for use with TASA, with the results from Inks B and C and Templates I–V also shown in Figure 3. Compared to Ink A, clusters with fewer nanorods were produced with Ink B regardless of the Template. This result is consistent with the larger nanorod size. In some cases, the low number of nanorods per cluster spot gave rise to very dim images such as with Template I. Additionally, the colorimetric responses varied quite a bit from cluster to cluster within a given array in the cases of the triangular wells (Template II) and small circular wells (Template III). In these cases, there were fewer nanorods per cluster (i.e., typically less than 30), which gave rise to anisotropic spectral responses. Larger arrays gave brightly colored responses (average brightness of 95.5 au for Template IV versus 73.6 au for Template I) due to the structural color imparted by the lattice plasmon resonance.

Compared to Inks A and B, Ink C – which is comprised of spherical NPs – gave somewhat uniform green responses for Templates I–III and V. This observation can be explained through the isotropic nature of the NPs. Still, TASA of Ink C with Template IV gave a tag with greater color variation from cluster to cluster compared to other tags created with Ink C. This finding is attributed to NPs being arranged in a larger array size where the variance in cluster filling and the larger array size influence individual cluster responses. Large area SEM images of tags from Inks A, B, and C are shown Figures S10–S19 (Supporting Information).

Our qualitative discussion provides some insights into the optical response of arrayed clusters of Au NPs with variable numbers, orientation, and shapes, with a more quantitative framework only possible by simulations. However, predicting the lattice surface plasmon resonance through simulations is a non-trivial task.[49,50] Fortunately, Adam, Seifert, and coworkers have previously reported finite-element method (FEM) simulations of arrayed clusters of Au NPs and nanorods to highlight coupling between plasmonic lattice modes and cluster-specific plasmons reflected in UV/Visible/NIR spectroscopy.[49] We summarize major findings from their FEM simulations in Table S3 (Supporting Information), selecting three cluster morphologies that resemble those observed from Inks A, B, and C. Example 1 consists of heptamers arising from spherical Au NPs. Example 2 consists of Au nanorod trimers where the nanorods are parallel to one another. Example 3 consists of Au nanorod tetramers with one rod transverse to the tips of three parallel nanorods. Schematics of these configurations, along with relevant peaks from their simulated spectra with arrayed spacings of 400 and 500 nm are summarized in Table S3 (Supporting Information). The spectra of the arrayed NP clusters are different from the NPs dispersed in solution on account of plasmonic coupling within the clusters and plasmonic lattice effects. Notably, the arrays of spherical NP clusters show red-shifting of the plasmonic modes with increasing lattice period, while the arrays of nanorod clusters show two resonances, with minimal shifting in transverse polarization with increasing lattice period and red-shifts in longitudinal polarization with increasing lattice period. Similar spectral changes with changes in NP cluster and lattice

period would be anticipated from our systems, although we often have more nanorods per clusters, giving rise to variability between NP clusters; such spectral changes correlate with the different colorimetric responses from the tags as well as highlight the modular nature of our tag design.

Considering the results obtained with Inks A–C and Templates I–V collectively, the promise of TASA in creating optical security tags is evident. Varied color responses were obtained from both different Templates and different Inks. This quality means that different lots of critical goods could be tagged with a selected TASA and that the tag could be readily redesigned by changing the Template features, Ink, or both to yield a different pattern and color response. Moreover, the systematic study presented in Figure 3 also illustrates that some Template-Ink combinations create qualitatively better tags in terms of uniformity of color responses within an array. To achieve tags with more uniform responses, NP size relative to the well dimensions should be considered. For example, the nanorods comprising Ink A have a smaller cross-sectional area (≈1200 nm^2) compared to those for Ink B (≈3400 nm^2) and are assembled in the stamp wells with many more nanorods per well, leading to little variance in colorimetric response within an individual stamp. As we will show, when variance from spot to spot is low, authentication to a lot (i.e., specific Ink/Tag) based on color analysis is possible.

2.2. Authentication of Unique Images

The optical images in Figure 3 suggest that visual inspection of a tag may be sufficient in some applications to authenticate a particular good (e.g., does the good contain a green tag?); however, a quantitative measure of the color response and array features would be appropriate in applications requiring a higher level of security, and of course, the quantitative readout should be reproducible when creating tags with the same Ink-Template combination (i.e., product lots). Toward this effort, a blob detection algorithm was developed to identify scattering responses from the images while excluding miscellaneous artifacts (e.g., scattering from isolated or randomly aggregated NPs). Then, color (RGB) values, array size, and well spacing were extracted from the detected blobs (Figure 4a; Figures S20–S24, Supporting Information for full details).

To check for color response similarity for tags belonging to the same lot, images from Ink A with Template III were selected with five different tag images shown (Figure 4b). Color was represented in a 24-bit standard RGB color space as a vector of three integers from 0–255, indicating the intensity of red, green, and blue color channels. The figure presents color histograms showing the proportion of blobs as a function of each RGB color channel value with a bin size of 18 along each color dimension. As the number of detected blobs vary for different images, depending on the filling fraction, the counts for blobs were normalized with the total number of blobs detected for each tag. Viewing the images shown in Figure 4b by eye may suggest some variability, which is also represented in the RGB analysis of each image. However, broadly, the normalized counts of blobs in the histograms for RGB intensity lie within similar intensity ranges for all images. Similarly, joint RGB responses represented in the 3-D scatter plot also cover a similar color space. Notably, slight differences in distribution can be observed for images 4 and 5 compared to image 1 in

Figure 4b, which can be attributed to variability in filling of some tags as a result of the manual fabrication process.

Next, to look at the color distribution from different tag categories, images from different Templates and Inks were analyzed. Figure 5 compares results from Ink A/Template I, Ink A/Template II, and Ink B/Template II, which were selected to illustrate changes in both the Ink and Template on color response. As anticipated, both RGB histograms and 3-D RGB scatter plots show an obvious shift in color space when the Template is changed as well as when the Ink is varied for the same Template. For Ink A in Template I versus Template II, an obvious shift in the intensity range for blue is observed, as the bins now populate lower intensities for contribution of blue. Changing Inks results in an even more drastic shift, where the population of all intensity ranges for red, green, and blue contributions shift. Notably, comparing 3-D scatter plots for Figure 5b,c shows how the RGB responses are more scattered for Ink B versus Ink A.

Additionally, the blob detection algorithm can discriminate between compromised tags and disrupted patterns from high-quality tags. Compromised tags may arise from poor fabrication techniques or a tamper attempt. Figure S25 (Supporting Information) shows three tag images from Ink A/Template V, with variable filling. For the tag with the highest filling fraction, the RGB analysis shows a high intensity in green (Figure S25A, Supporting Information). With slightly less filling, slight changes in the RGB distribution are evident (Figure S25B, Supporting InformationSupporting Information). Significantly, the blob detection algorithm is unable to detect tag boundaries when the filling fraction is very low, as in Figure S25C (Supporting Information), removing the tag from the data set.

The optical images contain features that can be traced back to production parameters and are used in classifying the images into predefined categories. Here, two approaches toward classification and authentication were evaluated. Method 1 is a traditional computer vision approach with hand engineered features, wherein information extracted from the blob detection algorithm was used to train a shallow neural network for subsequent classification of new images. In Method 2, a deep neural network, specifically, a Vision Transformer (ViT) model, is used to extract image features and a Support Vector Machine (SVM) for category prediction from the ViT features. Method 2 does not require the data extraction process with blob detection. An advantage is Method 1 has comparatively few model parameters, which offers some ability to explain results; however, limitations include that the neural network is limited to only select tag designs. In contrast, the deep neural network approach of Method 2 should be compatible with the highly modular nature of TASA to create tags, including when the tag dimensions and array size are varied.

For Method 1, a shallow neural network with five layers (one input layer, three internal layers, and one output layer), was trained with TensorFlow where the input data from tags (RGB values and RGB standard deviation) was split into training and test data, with 80% of the data used in training and 20% to test. Here, the data were extracted from tags created from Inks A-C collectively with the blob detection algorithm. Information on the training parameters can be found in the Supporting Information.

A Confusion Matrix Was Used To Evaluate And Visualize The accuracy of the neural network.[51,52] After training was complete, the test images were run through the network to produce a predicted (estimated) label for each image. These predictions are compared to the actual values, and the number of correct answers and incorrect answers are recorded for each tag category. These values are placed in a matrix where the columns represent the Ink predicted by the network, and the rows represent the actual Inks. Table 2 shows a 3 × 3 confusion matrix for classification of images from Inks A, B, and C. This confusion matrix shows values averaged over ten trials of training and testing by the neural network; results vary across trials both because of different random splits of the training and test data, and because neural network parameter training is stochastic. Of the actual Ink A tags, 84% were correctly predicted as Ink A, whereas 16% were estimated to be Ink B, and none were estimated as Ink C. Meanwhile 51% of Ink B tags and 79% of Ink C tags were correctly predicted. The overall prediction accuracy across all Inks was 71%.

To test the utility of the neural network for lot-level authentication, we used tags from Ink A, which showed different color responses as a function of Template, consistent filling fraction, and global color for each Template. Table S4 (Supporting Information) shows the resulting 5 × 5 confusion matrix from Method 1. The accuracy for Template categorizing is 51%. The error is mainly observed for Templates IV and V when they authenticated in the wrong categories. This inaccuracy arose because of their larger array and cluster spacings, for which the blob detection algorithm had difficulty extracting the number of cells accurately. These findings indicate that the method could potentially categorize tags based on Inks and into various lots with additional images for training, which would require automating the process of tag formation instead of manual TASA.

Method 2 used a deep neural network, a pretrained ViT-(ViTH/14) feature extraction model along with a linear SVM.[53] The ViT model takes an image and treats it as a sequence of fixed-size patches and uses a transformer architecture, originally developed for natural language processing, to process these patches. ViT leverages self-attention mechanisms to capture long-range dependencies between image patches, enabling the algorithm to recognize patterns and features within images. By pretraining on large datasets and fine-tuning for specific tasks, ViT has demonstrated competitive performance in tasks like image classification and object detection. For this experiment, a pretrained ViT-Huge model was used to convert each image into a single feature vector. The feature vectors for the training images were then used to train a linear SVM model. The ViT-Huge model was not modified or trained during the training process. For inference, the pretrained ViT-Huge model was used to extract features from test images, and the trained SVM was used to identify the category.

Table 3 shows the confusion matrix for Inks A, B, and C by the ViT model with values averaged over ten trails. Of the actual Ink A tags, 80% were correctly identified as Ink A and 20% were incorrectly identified as Ink B. For Inks B and C, 52% and 82% were correctly classified, respectively. Overall, this model had an accuracy of 71% of categorizing based on Inks. Table 4 shows the 5 × 5 confusion matrix from tags generated with Ink A from Templates I–V. For this 5-way classification problem, the ViT model had an impressively improved accuracy of 89%. 100% of tags from

Template I, 78% from Template II, 100% from Template III, 89% from Template IV, and 61% from Template V were correctly identified. Table 5 compares the accuracies of Method 1 and 2, where both methods categorize Inks with similar accuracies while Method 2 categorizes Templates with increased accuracy. These results highlight the utility of a deep neural networkwhenimageshavedifferentdimensions/featuresandhandengineered features become limiting. These studies also suggest Ink-Template combinations can be used for more specific lot-level identification after the initial, broader categorization based on Inks. These combinations allow for the creation of a multiplexed tag where information can be encrypted at multiple levels of tag generation.

Even though the accuracy of the algorithm is satisfactory for categorization based on Ink-Template combinations for proof-of-concept, we recognize that the robustness could be improved with a larger dataset to train the neural network. However, manual TASA limits the number of tags generated, and human handling can impact the quality of NP assembly (e.g., number of filled wells and NPs occupying non-cluster regions of the tag), particularly with regard to placement of the substrate and subsequent force required for lift-off. Mechanized roll-to-roll generation of analogous tags could be transformative to create precise arrays of NP clusters and to fully train the neural network, leading to classification with higher precision and speed. Notably, substantial efforts have been dedicated to scaling the production and reuse of Templates made of PDMS and related materials from master molds, without degradation of fine features.[54,55] We note that Inks comparable to those used in the manuscript are currently commercially available at modest costs (e.g., 8.8 USD/mL with an optical density of 1), which would bring Ink costs to << 0.01 $/tag; however, a full techno-economic analysis has not been undertaken.[56] Additional costs associated with tag production could include that of the polymer Template (<0.1$ per tag) used in the TASA process and labor costs for tag fabrication.[57] Moreover, TASA is compatible with a variety of substrates,[33–36] making printing of these tags onto different critical goods feasible, including rough and non-transparent surfaces where the light scattering from the arrayed NPs could be imaged in reflection mode.

We envision developing TASA tags for quick visual as well as spectroscopic analysis, e.g., by diffuse reflectance spectroscopy (DRS). We note that optimization of our approach is currently required to realize this version as TASA tags created in the same manner as those in Figure 4 show limited features by DRS (Figure S26, Supporting Information). This observation is consistent with the dilute nature of the NPs on the substrate relative to the capabilities of a commercial DRS setup. More over, deeplearning image analysis would capture features of the underlying substrate as well as the TASA-generated tag during training.[9]

Overall, these tags are detected in the visible wavelength range, which translates to a facile interrogation by microscopy methods that could potentially be integrated into hand-held smart phones, lowering the potential costs of authentication. We refer readers to Table S5 (Supporting Information) for a review of various anti-counterfeit tags and their properties as a function of the different classes of materials used to make them. Notably, each tag serves a different counterfeiting need, depending on the value of the critical good and the level of encryption required. Some printed tags use synthetically complex inks with the

requirement of excitation sources and fluorescence microscopes for a readout, increasing the cost of tag production, implementation, and authentication. A standout feature of Au Inks for TASA-generated tags is their stability, where other classes of materials experience photo-blinking and photo-bleaching. Moreover, compared to plasmonic PUFs, these tags are not created through a completely stochastic method given the template-directed assembly; this quality offers the advantage of visual tracking of optical responses by eye, over time, which would be non-trivial for randomly drop-casted dilute nanoparticles. Hence, these tags are ideal for quick screening of goods at various points of the supply chain.

3. Conclusion

Metal NP arrays prepared by TASA were fabricated and evaluated for use as robust and modular anti-counterfeit tags. The Template features (i.e., well dimensions and spacings) and the NP Inks (size and shape of NPs) were systematically varied to evaluate the feasibility of different combinations to create unique optical images that could serve as security tags. As we found, the observed colors and patterns could be readily imaged by dark-field microscopy with the specific response depending on NP size and shape as well as cluster size and array features. Uniform color responses arose when smaller nanorods organized in isotropic clusters, and variation was evident when larger nanorods angularly interacted within a cluster resulting in cluster anisotropy. Authentication protocols for Ink-Template combinations that gave uniform color responses were established. A comparison between a customized approach that involved feature extraction steps followed by classification with a shallow neural network versus a deep neural network approach operating with raw input image data showed higher accuracy for the latter. Collectively, this study establishes that NP cluster arrays created by TASA are suitable for optical security tags, opening the possibility for modular anti-counterfeit tags by TASA or other fabrication methods where cluster and array features can be readily varied.

4. Experimental Section

Synthesis and Characterization of NP Inks—Materials:

Gold (III) chloride trihydrate ($HAuCl_4 \bullet 3H_2O$, ≥99.9%), L-ascorbic acid (L-AA, BioXtra, ≥99.0%), poly(ethylene glycol) methyl ether thiol (PEG-6K-SH, av. Mn = 6000 g/mol), hexadecyltrimethylammonium bromide (CTAB, BioUltra, ≥99.0%), and sodium borohydride ($NaBH_4$, 99.99%) were purchased from Sigma–Aldrich. Cetyltrimethylammonium chloride (CTAC, ≥95.0%) and sodium oleate (NaOL, 97.0%) were purchased from TCI America. Ethanol (Absolute) was purchased from Pharmco-Aaper. Sodium hypochlorite solution (available chlorine 10−15%), acetone (ACS grade), hydrochloric acid (HCl, ≈37%), methanol (ACS grade), and isopropanol (IPA, ACS grade) were purchased from Macron. All scintillation vials were rinsed with ethanol and dried with air prior to use. Milli-Q ultrapure water (18.2 MΩ•cm) was used in all experiments. All chemicals were used as received. Glass slides were purchased from VWR. Silica wafers were purchased from Wafer Works (Shanghai) Corp.

Synthesis of Au Nanorods for Inks A and B:

Au nanorods were synthesized from a previously reported protocol with minor modifications.[10] The synthesis occurs in two steps: seed formation and growth. First, 25 μL of 100 m"M $HAuCl_4$ was added to 5 mL of 200 mM CTAB solution and 4.75 mL of water in a 20 mL scintillation vial. Next, 1200 μL of 10 mM $NaBH_4$ was diluted with 800 μL of water. 1 mL of the diluted $NaBH_4$ was rapidly added to the growth solution under vigorous stirring (1200 rpm). After 2 min of stirring, the seed solution was left undisturbed for 30 min. Next, growth solution was prepared with 1.23 g of CTAC, 0.3086 g of NaOL, and 50 mL of water, which were dissolved in a 250 mL flask at 50 °C. After cooling the solution to 30 °C, 2.4 mL of 4 mM $AgNO_3$ was added to the growth solution, which was left undisturbed for 15 min. For each sample, 10 mL solutions containing 100 μL of 100 mm $HAuCl_4$, 9.9 mL of growth solution, and 10 mL water were prepared in a scintillation vial. After stirring for 120 min, a volume of HCl was added to the mixture. After another 15 min of slow stirring (400 rpm), 50 μL of 64 mM L-AA was added to the solution, which was vigorously stirred at 1200 rpm for 30 s. Finally, a defined volume of seed solution was added to the solution, and the reaction was stirred for 30 s. The conditions to make rods of different aspect ratios, Inks A and B (presented in Figure 2 and Figure S1, Supporting Information), are in Table S2 (Supporting Information). The reactions were left undisturbed for 12 h. To concentrate and purify, samples were centrifuged at 10 000 rpm, supernatant discarded, and pellet redispersed in 1 mL of water.

Synthesis of Quasi-spherical Au NPs for Ink C:

Au NPs with quasi-spherical shape were synthesized from a previously reported protocol with minor modifications.[58] The synthesis involved the formation of a seed solution that was used to synthesize 10 nm Au NPs and, subsequently, to grow larger Au NPs.

Au seeds were formed by adding 50 μL of a 0.05 M $HAuCl_4$ solution to 5 mL of a 0.1 m CTAC solution to which 200 μL of a freshly prepared 0.02 M $NaBH_4$ (7.6 mg/10 mL) were rapidly added while stirring (12 000 rpm). Stirring was stopped after 3 min, after which the sample was diluted tenfold in CTAC 100 mm. Next, the 10 nm Au NPs were synthesized by adding 900 μL of the seed solution and 40 μL of 0.1 m ascorbic acid to 10 mL of 25 mm CTAC solution. Afterward, 50 μL of a 0.05 m $HAuCl_4$ solution was added under vigorous stirring. The mixture was left undisturbed for 1 h to be finally used for seeded growth. To form Au NP of ˜60 nm, 25 μL of 10 nm Au NPs and 40 μL of 0.1 m L-AA were added to 10 mL of a 25 mm CTAC solution. 10 μL of a dilute sodium hypochlorite solution (1 to 1.5 wt. % of available chlorine) was injected into 10 mL of grown NPs under rapid stirring. After 5 min, 2.5 μL of 0.05 m $HAuCl_4$ solution were added. The mixture was left undisturbed at 30 °C until oxidation was completed in ≈10 h.

PEGylation of Metal NPs:

To attain a metal NP solution of high concentration, three batches of NPs made by the same protocols were combined, concentrated by centrifugation, and redispersed in 2 mM CTAC. Ligand exchange was performed with thiolated PEG6K, which was added to the Au NP solutions; the NP solutions were estimated to be 10 mM (estimated at Abs_{400} for Au).[59–61] 1 mg mL^{-1} of PEG was added to 1 mm AuNP solution. The PEGylated samples

were collected by centrifugation, and the supernatant was discarded to remove excess PEG, followed by redispersion in 2 mM CTAC. The stock NP solutions were estimated to be 40 mM (estimated at Abs_{400} for Au).

Template-Assisted Self-Assembly of Metal NPs—Preparation of NP Solutions for TASA:

Colloidal solutions of Au NPs were prepared for TASA from the initial Au NP stock solutions. The Au NPs were resuspended in a 55:45 ethanol: water mixture with a CTAC concentration of 200 μM. Final Au concentrations were estimated to be 15 mm based on their absorbance at 400 nm.

Preparation of Glass Substrates for Assembly Transfer:

Borosilicate microscope coverslips (Menzel, #1.5) with dimensions of 24 × 50 mm^2 were cut to dimensions 1.5 × 1.5 cm^2 and used as substrates. Substrates were cleaned with Hellmanex III solution, followed by sonication in isopropanol and water for 30 min each. The substrates were dried in a stream of nitrogen followed by treatment with an air plasma at an energy of 216 J.

TASA of AuNPs:

The main steps of the assembly process are shown in Figure S9 (Supporting Information). A 2 μL solution of selected PEGylated Au NPs was drop-cast onto the x-PDMS/PDMS Template as close to the patterned surface as possible. After 1 min of preassembly time, the hydrophilized glass substrate was slowly lowered onto the Template, starting at a 45° angle. After a drying time in ambient conditions of 12 h, the glass substrate was removed, transferring the assembled array to the glass substrates. The Templates can be reused once after cleaning with adhesive tape, followed by rinsing with IPA and water.

Nanoparticle Characterization:

All NPs were characterized on JEOL JEM 1010 TEM that was operated at 80 keV, and images were collected with a ROM CCD camera. TEM samples were drop-cast onto carbon-coated copper TEM grids after the sample was washed 1–2 times (TEM analysis was performed prior to PEGylating). The LSPR response of the metal NPs in solution was evaluated with a Varian CARY 100 Bio UV–vis spectrophotometer with a quartz cuvette and a background scan of water. For SEM images of Au NP arrays after TASA, a 10 nm layer of Au/Pd as sputtercoated (Denton Desktop V) onto the sample to minimize charging effects. The arrays were analyzed with an SEM (Zeiss Auriga 60) at an accelerating voltage of 10 kV.

Diffuse Reflectance Spectroscopy:

Diffuse reflectance spectroscopy (DRS) was conducted on a Varian Cary 100 Bio UV–vis spectrophotometer equipped with a Cary 301 DR accessory. $BaSO_4$ powder was pressed onto a cylindrical powder holder with dimensions of 3 mm height × 17 mm diameter. $BaSO_4$ was used as the 100% reflectance reference, in front of which glass substate with sample, was attached.

Dark-field Optical Microscopy:

Optical images of NP arrays prepared by TASA were acquired with an Olympus GX53–1-2 inverted microscope equipped with an color CCD camera. Samples were illuminated with a white LED source, and images were captured with STREAM Basic software (Olympus). Images were acquired in reflectance mode in which the system can easily alternate between dark- and bright-field microscopy with objectives having the following specifications: 10x (NA 0.3, WD 6.5 mm, air), 20x (NA 0.45, WD 3 mm, air), 50x (NA 0.8, WD 1 mm, air), and 100x (NA 0.9, WD 1 mm, air). Fine positioning controls were provided by the NanoDrive piezoelectric stage purchased through Mad City Labs. The tag patterns were imaged at magnification 100x in dark-field mode. The acquisition and ISO settings of the camera were set at 1 s and 200, respectively, for all images of the tags.

Supplementary Material

Refer to Web version on PubMed Central for supplementary material.

Acknowledgements

For S.E.S. and M.I., this work was funded in part by Research Corporation for Scientific Advancement through their Frontiers in Research Excellence & Discovery Award. S.E.S., M.I., Z.M. and D.J.C. also acknowledge support from Indiana University. M.I. acknowledges a Kindig Fellowship at Indiana University. M.I. also thanks Dr. Zachary Woessner, Dr. Joshua Smith, and Nayana Christudas Beena for insightful discussions. For S.C.J. and S.-Y.H, this work was supported in part by NIH R35 GM141922 and NSF CHE-0923064. The authors thank the Indiana University Nanoscale Characterization Facility for use of its instruments. The authors would like to thank the staff of the Nanoscale Characterization Facility (Dr. Yi Yi and Dr. Jun Chen) and Electron Microscopy Center (Dr. Barry Stein, and Dr. Xun Zhan) at Indiana University for instrument training.

Data Availability Statement

The data that support the findings of this study are available from the corresponding author upon reasonable request.

References

[1]. Wang L, Hasanzadeh Kafshgari M, Meunier M, Adv. Funct. Mater 2020, 30, 2005400.

[2]. Singh SK, Mazumder S, Vincy A, Hiremath N, Kumar R, Banerjee I, Vankayala R, ACS Appl. Nano Mater 2023, 6, 1508.

[3]. Chow TH, Li N, Bai X, Zhuo X, Shao L, Wang J, Acc. Chem. Res 2019, 52, 2136. [PubMed: 31368690]

[4]. Akiyoshi K, Tanaka YY, Ishida T, Shimura T, Tatsuma T, ACS Appl. Nano Mater 2018, 1, 5994.

[5]. Farooq S, Rativa D, de Araujo RE, Plasmonics 2023, 18, 2475.

[6]. Pincelli T, Vasileiadis T, Dong S, Beaulieu S, Dendzik M, Zahn D, Lee S-E, Seiler H, Qi Y, Xian RP, Maklar J, Coy E, Mueller NS, Okamura Y, Reich S, Wolf M, Rettig L, Ernstorfer R, Adv. Mater 2023, 35, 2209100.

[7]. Hutter E, Fendler JH, Adv. Mater 2004, 16, 1685.

[8]. Willets KA, Van Duyne RP, Annu. Rev. Phys. Chem 2007, 58, 267. [PubMed: 17067281]

[9]. Smith JD, Reza MA, Smith NL, Gu J, Ibrar M, Crandall DJ, Skrabalak SE, ACS Nano 2021, 15, 2901. [PubMed: 33559464]

[10]. Ye X, Zheng C, Chen J, Gao Y, Murray CB, Nano Lett. 2013, 13, 765. [PubMed: 23286198]

[11]. Carbone L, Cozzoli PD, Nano Today 2010, 5, 449.

[12]. Kang H, Buchman JT, Rodriguez RS, Ring HL, He J, Bantz KC, Haynes CL, Chem. Rev 2019, 119, 664. [PubMed: 30346757]

[13]. Lee S, Sim K, Moon SY, Choi J, Jeon Y, Nam J-M, Park S-J, Adv. Mater 2021, 33, 2007668.

[14]. Ha M, Kim J-H, You M, Li Q, Fan C, Nam J-M, Chem. Rev 2019, 119, 12208. [PubMed: 31794202]

[15]. Naoum-Sawaya J, Elhedhli S, De Carvalho P, Eur. J. Oper. Res 2023, 311, 373.

[16]. Javaid M, Haleem A, Singh RP, Suman R, Cyber Secur. Appl 2023, 1, 100016.

[17]. Kae-Nune N, Pesseguier S, In 2013 Design, Automation & Test in Europe Conference & Exhibition (DATE), IEEE, Grenoble, France 2013, pp 1131.

[18]. Arppe R, Sørensen TJ, Nat. Rev. Chem 2017, 1, 1.

[19]. Shah RY, Prajapati PN, Agrawal YK, J. Adv. Pharm. Technol. Res 2010, 1, 368. [PubMed: 22247875]

[20]. Wang M, Duong B, Fenniri H, Su M, Nanoscale 2015, 7, 11240. [PubMed: 26073745]

[21]. Gooch J, Goh H, Daniel B, Abbate V, Frascione N, Anal. Chem 2016, 88, 4456. [PubMed: 27010696]

[22]. Abdollahi A, Roghani-Mamaqani H, Razavi B, Salami-Kalajahi M, ACS Nano 2020, 14, 14417. [PubMed: 33079535]

[23]. Smith AF, Skrabalak SE, J. Mater. Chem. C 2017, 5, 3207.

[24]. Zhao Z, Chamele N, Kozicki M, Yao Y, Wang C, J. Mater. Chem. C 2019, 7, 6099.

[25]. Chi Z, Valehi A, Peng H, Kozicki M, Razi A, IEEE Access 2020, 8, 118623.

[26]. Ibrar M, Skrabalak SE, Small Struct. 2021, 2, 2100043.

[27]. Anderson BR, Gunawidjaja R, Eilers H, Appl. Opt 2017, 56, 2863. [PubMed: 28375254]

[28]. Caligiuri V, Patra A, De Santo MP, Forestiero A, Papuzzo G, Aceti DM, Lio GE, Barberi R, De Luca A, ACS Appl. Mater. Interfaces 2021, 13, 49172. [PubMed: 34632778]

[29]. Kim J, Yun JM, Jung J, Song H, Kim J-B, Ihee H, Nanotechnology 2014, 25, 155303. [PubMed: 24651153]

[30]. Lee JB, Walker H, Li Y, Nam TW, Rakovich A, Sapienza R, Jung YS, Nam YS, Maier SA, Cortés E, ACS Nano 2020, 14, 17693. [PubMed: 33270433]

[31]. Gupta V, Probst PT, Goßler FR, Steiner AM, Schubert J, Brasse Y, König TAF, Fery A, ACS Appl. Mater. Interfaces 2019, 11, 28189. [PubMed: 31298836]

[32]. Zhang H, Bu X, Yip S, Liang X, Ho JC, Adv. Intell. Syst 2020, 2, 1900085.

[33]. Alba M, Pazos-Perez N, Vaz B, Formentin P, Tebbe M, Correa-Duarte MA, Granero P, Ferré-Borrull J, Alvarez R, Pallares J, Fery A, de Lera AR, Marsal LF, Alvarez-Puebla RA, Angew. Chem., Int. Ed 2013, 52, 6459.

[34]. Matricardi C, Hanske C, Garcia-Pomar JL, Langer J, Mihi A, Marzán L, ACS Nano 2018, 12, 8531. [PubMed: 30106555]

[35]. Hanske C, González-Rubio G, Hamon C, Formentín P, Modin E, Chuvilin A, Guerrero-Martínez A, Marsal LF, Liz-Marzán LM, J. Phys. Chem. C 2017, 121, 10899.

[36]. Garg A, Nam W, Zhou W, ACS Appl. Mater. Interfaces 2020, 12, 56290. [PubMed: 33283507]

[37]. Murphy CJ, Sau TK, Gole AM, Orendorff CJ, Gao J, Gou L, Hunyadi SE, Li T, J. Phys. Chem. B 2005, 109, 13857. [PubMed: 16852739]

[38]. Sau TK, Murphy CJ, J. Am. Chem. Soc 2004, 126, 8648. [PubMed: 15250706]

[39]. Yockell-Lelièvre H, Lussier F, Masson J-F, J. Phys. Chem. C 2015, 119, 28577.

[40]. Fernandez-Cuesta I, Palmarelli AL, Liang X, Zhang J, Dhuey S, Olynick D, Cabrini S, J. Vac. Sci. Technol. B Nanotechnol. Microelectron. Mater. Process. Meas. Phenom 2011, 29, 06f801.

[41]. Halas NJ, Lal S, Chang W-S, Link S, Nordlander P, Chem. Rev 2011, 111, 3913. [PubMed: 21542636]

[42]. Rodriguez SRK, Schaafsma MC, Berrier A, Rivas G, Phys. B Condens. Matt 2012, 407, 4081.

[43]. Kravets VG, Kabashin AV, Barnes WL, Grigorenko AN, Chem. Rev 2018, 118, 5912. [PubMed: 29863344]

[44]. Cherqui C, Bourgeois MR, Wang D, Schatz GC, Acc. Chem. Res 2019, 52, 2548. [PubMed: 31465203]

[45]. DeVoe H, J. Chem. Phys 1964, 41, 393.

[46]. Zou S, Schatz GC, J. Chem. Phys 2004, 121, 12606. [PubMed: 15606284]

[47]. Yurkin MA, Hoekstra AG, J. Quant. Spectrosc. Radiat. Transf 2007, 106, 558.

[48]. Scarabelli L, Vila-Liarte D, Mihi A, Liz-Marzán LM, Acc. Mater. Res 2021, 2, 816.

[49]. Charconnet M, Korsa MT, Petersen S, Plou J, Hanske C, Adam J, Seifert A, Small Methods 2023, 7, 2201546.

[50]. Yan B, Boriskina SV, Reinhard BM, J. Phys. Chem. C 2011, 115, 24437.

[51]. Caelen O, Ann. Math. Artif. Intell 2017, 81, 429.

[52]. Susmaga R, in Intelligent Information Processing and Web Mining, (Eds: Kłopotek MA, Wierzchoń ST, Trojanowski K), Springer, Berlin, Heidelberg 2004, pp. 107–116.

[53]. Dosovitskiy A, Beyer L, Kolesnikov A, Weissenborn D, Zhai X, Unterthiner T, Dehghani M, Minderer M, Heigold G, Gelly S, Uszkoreit J, Houlsby N, arXiv 2021, 10.48550/arXiv.2010.11929.

[54]. Sung SH, Yoon H, Lim J, Char K, Small 2012, 8, 826. [PubMed: 22279040]

[55]. Bourguignon N, Olmos CM, Sierra-Rodero M, Peñaherrera A, Rosero G, Pineda P, Vizuete K, Arroyo CR, Cumbal L, Lasorsa C, Perez MS, Lerner B, J. Polym. Sci. Part B Polym. Phys 2018, 56, 1433.

[56]. PEG Functionalized Gold Nanoparticles – Nanopartz, https://www.nanopartz.com/gold-nanoparticles-peg.asp, (accessed: April 2024).

[57]. Polydimethylsiloxane, dihydroxy terminated – scipoly.com. https://scipoly.com/shop/polydimethylsiloxane-dihydroxy-terminated-11/, (accessed: April 2024).

[58]. Hamon C, Novikov S, Scarabelli L, Basabe-Desmonts L, Liz-Marzán LM, ACS Nano 2014, 8, 10694. [PubMed: 25263238]

[59]. Jain PK, Lee KS, El-Sayed IH, El-Sayed MA, J. Phys. Chem. B 2006, 110, 7238. [PubMed: 16599493]

[60]. Hu ZJ, Hou S, Ji YL, Wen T, Liu WQ, Zhang H, Shi XW, Yan J, Wu XC, AIP Adv 2014, 4, 117137.

[61]. Hanske C, Hill EH, Vila-Liarte D, González-Rubio G, Matricardi C, Mihi A, Liz-Marzán LM, ACS Appl. Mater. Interfaces 2019, 11, 11763. [PubMed: 30844239]

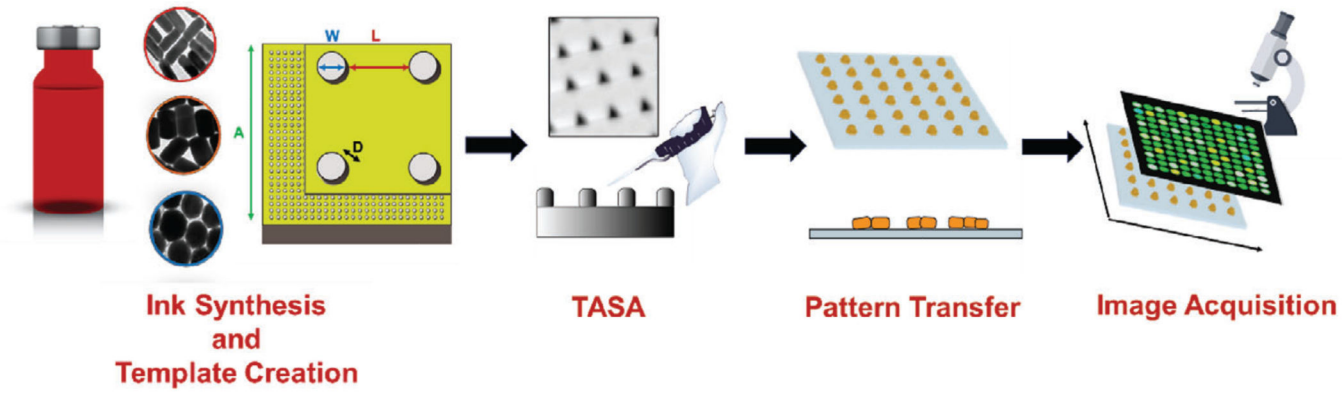

Figure 1.

Scheme for tag fabrication that involves four steps. First is selection and synthesis of plasmonic NP Inks and design of Templates and their replication. Second, Inks are drop-cast onto Templates for TASA. Third, the pattern is transferred onto a substrate through lift-off. Finally, the scattering response through a dark-field optical microscope is captured by an interfaced CCD camera.

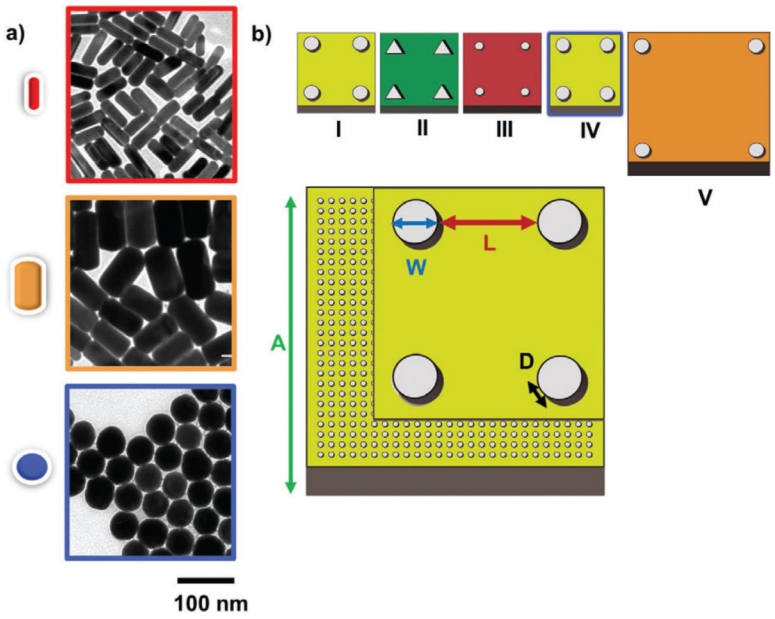

Figure 2.

a) TEM images for Au NP Inks A, B, and C, with cartoon models of the NPs used as reference in future images. b) Schematic representations of Templates I–V where W is the well width, D is the well depth, L is the spacing between wells, and A is the array size.

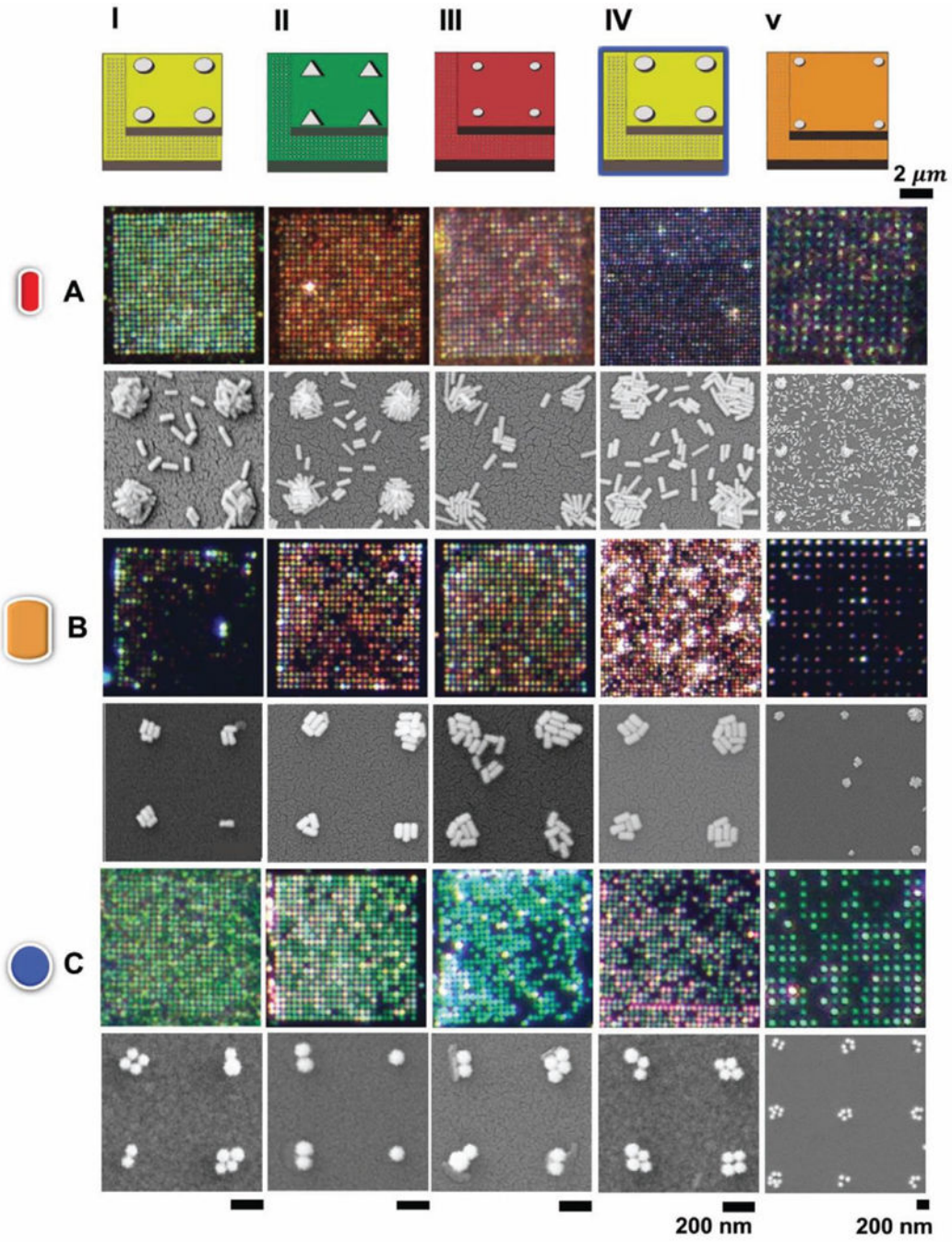

Figure 3.

This figure is organized as a grid where the top row shows schematics of the five Templates described in Figure 2. The second row shows dark-field images from the TASA of Ink A with Templates I–V. Below are the corresponding SEM images for the TASA of Ink A with Templates I–V. Similarly, the fourth and fifth rows show dark-field images and SEM images, respectively, from TASA of Ink B with Templates I–V. The sixth and the seventh rows show dark-field and SEM images, respectively, from TASA of Ink C from Templates I–V. The scale bar on the top is for all the dark-field images. Scale bars at the bottom are for

(left) SEM images from Templates I–IV and (right) for all SEM images in column V from Template V.

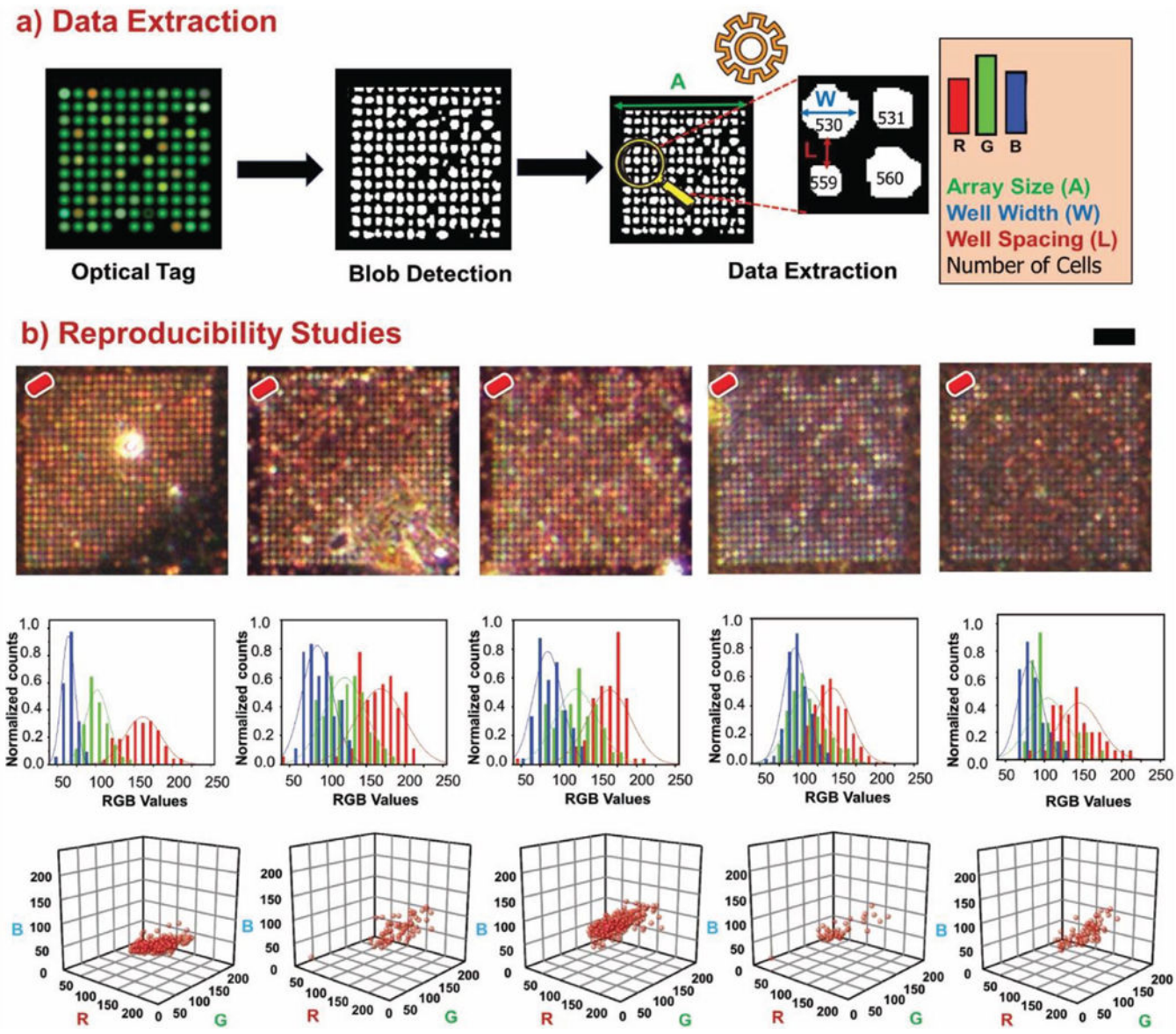

Figure 4.

a) Data extraction: An optical image of a tag is collected, and a blob detection algorithm is used to identify clusters and extract RGB values from each cluster in addition to array size (A), average well width (W), average well spacing (L), and number of cells for an array. B) Reproducibility study: Top Row) From left to right, dark-field optical microscopy images from 5 different tags created by the deposition of Ink A with Template III. Scale bar represents 2 μm. Middle Row) RGB histograms arising from the corresponding tags above, where the bin height corresponds to the primary color intensity for a particular intensity range normalized to the total counts of blobs detected by the algorithm. The bin width of the histograms is 18. These histograms show the RGB color contribution and distribution in the detected blobs for each tag. Normal distributions group the R, G, and B intensity histograms. Bottom Row) 3-D scatter plots of the RGB responses from blob detection analysis of the corresponding tag above.

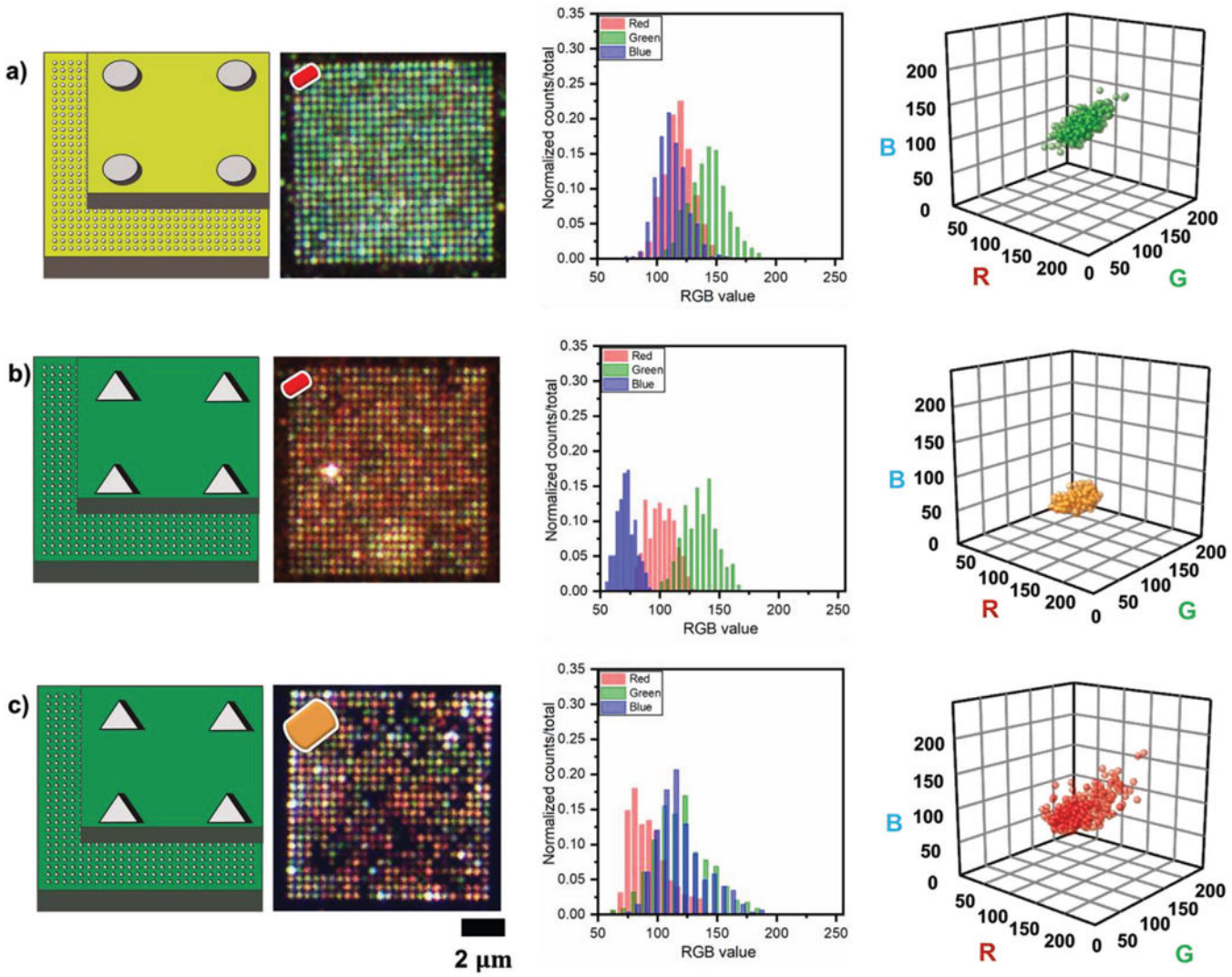

Figure 5.

a) Left: Schematic of Template I and dark-field image from the tag created with Ink A and Template I. Middle: Corresponding RGB histogram. Right: Corresponding 3-D scatter plot of RGB responses. b) Left: Schematic of Template II and dark-field image from tag created with Ink A and Template II. Middle: Corresponding RGB histogram. Right: Corresponding 3-D scatter plot of RGB responses. c) Left: Schematic of Template II and dark-field image from tag created with Ink B and Template II. Middle: Corresponding RGB histogram. Right: Corresponding 3-D scatter plot of RGB responses.

Table 1.

Summary of topologically patterned x-PDMS/PDMS Templates used with TASA of the Au NP Inks. Table summarizes Template dimensions in nanometers.

Template	Array Size (A)	Well Shape	Well Width (W) [nm]	Well Depth (D) [nm]	Spacing (L) [nm]
I	25 × 25	Circle	240	66	500
II	25 × 25	Triangle	180	50	500
III	25 × 25	Small Circle	100	30	500
IV	100 × 100	Circle	180	50	500
V	25 × 25	Circle	240	66	1000

Table 2.

A 3 × 3 confusion matrix for predictions from Method 1 for Inks A, B, and C, showing for each actual Ink (rows), the distribution over Inks estimated by the model (columns).

		Predicted Values		
		Ink A	**Ink B**	**Ink C**
Actual Values	Ink A	0.84	0.16	0.00
	Ink B	0.47	0.51	0.02
	Ink C	0.12	0.08	0.79

Table 3.

A 3 × 3 confusion matrix for predictions from Method 2, the ViT model, for Inks A, B, and C. Rows represent actual conditions whereas columns represent predicted results.

		Predicted Values		
		Ink A	**Ink B**	**Ink C**
Actual Values	Ink A	0.80	0.20	0.00
	Ink B	0.48	0.52	0.00
	Ink C	0.07	0.11	0.82

Table 4.

A 5 × 5 confusion matrix for tags from Ink A in Templates I-V from Method 2, the ViT model.

		Predicted Values				
		I	**II**	**III**	**IV**	**V**
Actual Values	I	1.00	0.00	0.00	0.00	0.00
	II	0.00	0.78	0.00	0.22	0.00
	III	0.00	0.00	1.00	0.00	0.00
	IV	0.04	0.07	0.00	0.89	0.00
	V	0.34	0.00	0.00	0.06	0.61

Table 5.

Accuracies for Ink-based authentication (Inks A, B and C in Template I) and Template-based authentication (Ink A in Template I-V) for Methods I and II.

	Matrix Type	
Method	[3 × 3]	[5 × 5]
I	0.71	0.51
II	0.71	0.89